

# A CFD-BEM coupling technique for low Mach number flow induced noise

P. Croaker (1), N. Kessissoglou (1), S. Marburg (2)

(1) School of Mechanical & Manufacturing Engineering, The University of New South Wales, Sydney, NSW 2052, Australia  
(2) LRT4 – Institute of Mechanics, Universität der Bundeswehr München, D-85579 Neubiberg, Germany

## ABSTRACT

A technique to couple computational fluid dynamics (CFD) and boundary element method (BEM) models is proposed that allows the total sound pressure field produced by low Mach number flow past a rigid body to be predicted. An incompressible CFD solver is used to calculate the transient hydrodynamic flow field. Acoustic sources based on Lighthill's analogy are then extracted from the flow field data. The CFD/BEM coupling technique is used to compute the acoustic field incident on the body. The incident acoustic field is calculated based on a near-field solution of Lighthill's analogy, which employs numerical techniques to accurately evaluate singular and near-singular integrals. This incident field is combined with a BEM model of the cylinder to predict the scattered sound pressure field. The results from this CFD/BEM coupling technique are presented for flow past a circular cylinder with Reynolds number,  $Re_D=100$  and Mach number,  $M=0.02$ . The directivity of the sound pressure field at the vortex shedding frequency is compared with results of alternate methods available in the literature.

## INTRODUCTION

Lighthill (1952, 1954) reformulated the Navier-Stokes equation into a wave equation that represents the acoustic source generation by fluid motion and the propagation of these acoustic sources. He derived an acoustic analogy that demonstrates sound generated by a turbulent fluid flow is equivalent to the sound generated by a distribution of acoustic quadrupoles computed from the instantaneous velocity fluctuations. The acoustic sources are extracted from the transient flow field data and then a wave equation, derived from Lighthill's acoustic analogy, is solved to predict the propagation of these acoustic sources. Curle (1955) extended Lighthill's acoustic analogy to include the effect of stationary boundaries present in the turbulent flow on the sound generation. He showed that the contribution of a stationary rigid body on the sound generated by unsteady flow is equivalent to a surface distribution of acoustic dipoles computed from the instantaneous pressure fluctuations on the body. Powell (1964) demonstrated that forces acting on a rigid body due to the fluctuating hydrodynamic pressure cannot produce acoustic fluctuations as the boundary is fixed and cannot vibrate. Instead, the body causes diffraction and scattering of the acoustic waves generated by the flow noise sources and this significantly amplifies the sound pressure. Gloerfelt *et al.* (2005) successfully demonstrated that the surface distribution of dipoles from Curle's analogy is equivalent to the scattering of sound waves generated by the volume distribution of quadrupoles by the rigid surface. Hence, these surface integrals only represent an equivalent source and do not provide any insight into the actual acoustic sources generated by the flow or the hydrodynamic mechanisms that cause them.

For an acoustically compact body, Curle's analogy provides an accurate and efficient way to predict the sound scattered by a body immersed in a fluctuating flow field. For low Mach number flows past an acoustically compact body, a flow field predicted using either a compressible or an incompressible form of the fluid dynamics equations will produce accurate acoustic results with Curle's analogy. However, if the body is not acoustically compact, Curle's analogy does not accurately predict the scattered sound field unless the compressibility of the fluid is included in the hydrodynamic analysis (Schram, 2009; Khalighi *et al.*, 2010).

For low Mach number flow induced noise computations it is incredibly challenging and computationally impractical to include the fluid compressibility in the hydrodynamic analysis (Khalighi, 2010). Schram (2009) devised a BEM extension of Curle's analogy for non-compact bodies at low Mach numbers. The pressure was decomposed into acoustic and hydrodynamic components. Then, a boundary integral equation was developed by splitting the volume sources into near-field and far-field regions. However, Khalighi (2010) points out that there is no clear way to split the source field into near-field and far-field regions. In contrast, Khalighi *et al.* (2010) developed a boundary integral equation from Lighthill's wave equation and solved this using BEM. In their work the volume distribution of quadrupole sources in the flow field act as the acoustic sources and no assumptions about the compactness of the source region is made. The approach of Khalighi *et al.* (2010) is an excellent method for predicting low Mach number flow induced noise in the presence of both acoustically compact or non-compact bodies. However, in their approach the hydrodynamic noise sources are incorporated directly in their BEM formulation. Hence they have had to develop their own BEM solver to predict the scattered acoustic field. In this paper a different approach is adopted.

This paper presents a method to couple a CFD analysis of the hydrodynamic flow field past a body with a BEM analysis of the scattering of the acoustic waves by the body. This coupling is achieved by extracting acoustic sources from the flow field and calculating the propagation of the resulting acoustic waves from these sources to the body. The incident acoustic field is then applied to a BEM model of the body and the scattered acoustic field is predicted. The main advantage of this approach over that developed by Khalighi *et al.* (2010) is that, in this work, the acoustic wave propagation from the flow induced noise sources to the body is decoupled from the scattering of these waves by the body. Hence, any existing BEM solver can be used to predict the acoustic scattering. The CFD-BEM coupling technique is used to predict the far-field sound pressure produced by the volumetric quadrupole sources arising from laminar flow past a cylinder at a Reynolds number,  $Re_D=100$  and Mach number,  $M=0.02$ .

## NUMERICAL METHODS

### Incident Field from Lighthill's Acoustic Analogy

To calculate the incident field on a body, the acoustic pressure and pressure gradient on the body due to direct radiation of the flow induced noise sources is required. This acoustic pressure and pressure gradient must be calculated neglecting the diffracting effect of the body on the sound waves. Here, the acoustic pressure and pressure gradient are predicted based on Lighthill's acoustic analogy as given by (Lighthill 1952,1954):

$$\frac{\partial^2 \rho}{\partial t^2} - c_0^2 \frac{\partial^2 \rho}{\partial x_i^2} = \frac{\partial^2 T_{ij}}{\partial x_i \partial x_j} \quad (1)$$

where  $\rho$  is the fluid density and  $c_0$  is the speed of sound in the medium at rest.  $T_{ij}$  is the Lighthill tensor and is given by:

$$T_{ij} = \rho u_i u_j + (p - c_0^2 \rho) \delta_{ij} - \tau_{ij} \quad (2)$$

where  $p$  is the pressure,  $u_i$  and  $u_j$  are the  $i^{\text{th}}$  and  $j^{\text{th}}$  components of the velocity vector respectively,  $\delta_{ij}$  is the Kronecker delta and  $\tau_{ij}$  is the viscous stress tensor. The first term on the right hand side of equation (2) represents the contribution due to the Reynolds stresses. The second term relates to sound generation by non-isotropic processes and the third term represents the contributions due to viscous stresses. The present work is for low Mach number flows. For such a flow regime, it is reasonable to approximate Lighthill's tensor by:

$$T_{ij} = \rho_0 u_i u_j \quad (3)$$

where  $\rho_0$  is the incompressible fluid density. Khalighi (2010) has demonstrated that, for low Reynolds flows, the viscous stress contribution cannot be neglected. They showed that the viscous stresses on the body act as a dipole sound source. Hence, the viscous stresses must be taken into account for the case considered here. Rather than including the viscous stress in equation (3), the effect of the viscous stress on far-field sound pressure is considered separately by considering a surface distribution of shear stress dipoles and applying Curle's analogy (Curle, 1955). In what follows, a harmonic time dependence of  $e^{-i\omega t}$  has been assumed. It is assumed that a region of space,  $\Omega$ , with boundary  $\Gamma$ , contains a non-zero, spatially varying distribution of Lighthill's tensor. An integral equation for calculating the density at a field point,  $\mathbf{x}$ , can be expressed as (Lighthill, 1952):

$$\hat{\rho}(\mathbf{x}, \omega) = \frac{1}{c_0^2} \int_{\Omega} \frac{\partial^2 \hat{T}_{ij}(\mathbf{y}, \omega)}{\partial y_i \partial y_j} \hat{G}_h(\mathbf{x}, \mathbf{y}) d\mathbf{y} \quad (4)$$

where:

$$\hat{G}_h(\mathbf{x}, \mathbf{y}) = \frac{e^{ik_a r}}{4\pi r} \quad (5)$$

is the harmonic free field Green's function,  $k_a$  is the acoustic wavenumber,  $\mathbf{y}$  is the source point and  $r = |\mathbf{x} - \mathbf{y}|$ .  $\hat{T}_{ij}$  and  $\hat{\rho}$  represent the Fourier transforms of  $T_{ij}$  and  $\rho$ , respectively, and  $\bar{i}$  is the imaginary unit. Using  $\hat{\rho}_a = c_0^2 \hat{\rho}$ , an expression for the acoustic pressure,  $\hat{p}_a$ , is given by:

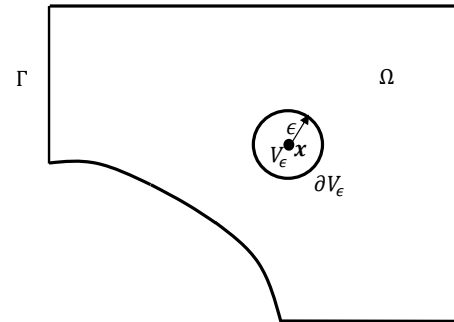
$$\hat{p}_a(\mathbf{x}, \omega) = \int_{\Omega} \frac{\partial^2 \hat{T}_{ij}(\mathbf{y}, \omega)}{\partial y_i \partial y_j} \hat{G}_h(\mathbf{x}, \mathbf{y}) d\mathbf{y} \quad (6)$$

From equation (6), the gradient of the acoustic pressure in the  $k^{\text{th}}$  direction, is then given by:

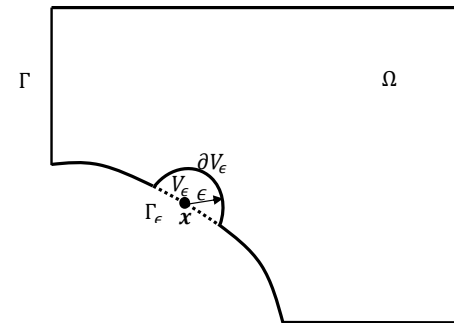
$$q_{\hat{a},k}(\mathbf{x}, \omega) = \frac{\partial \hat{p}_a(\mathbf{x}, \omega)}{\partial x_k} = \int_{\Omega} \frac{\partial^2 \hat{T}_{ij}(\mathbf{y}, \omega)}{\partial y_i \partial y_j} \frac{\partial \hat{G}_h(\mathbf{x}, \mathbf{y})}{\partial x_k} d\mathbf{y} \quad (7)$$

The expressions given by equations (6) and (7) contain the double spatial derivative of the Lighthill tensor. Crighton (1993)

suggests that the error caused by differentiating the acoustic sources can overwhelm the real sound at low Mach numbers. Hence it is standard practice to transfer the derivatives from Lighthill's tensor onto the Green's function by applying the divergence theorem. The Green's function is singular when  $\mathbf{x} = \mathbf{y}$ . To apply the divergence theorem to a function containing a singularity, a small spherical volume,  $V_\epsilon$ , of radius  $\epsilon$  and bounded by the surface  $\partial V_\epsilon$ , is excluded around the field point. When the field point lies on the boundary,  $\Gamma$ , the spherical exclusion neighbourhood intersects the boundary, with the vanishing boundary patch inside the spherical volume represented by  $\Gamma_\epsilon$ . The domain and boundaries remaining after the removal of this spherical volume are depicted in Figure 1.



(a) Field point in domain interior



(b) Field point on domain boundary

Figure 1: Domain with exclusion neighbourhood

### Domain Discretisation

The source region is divided into discrete cells and in turn these cells are partitioned into two sets corresponding to:

1.  $\Omega_s$ , representing the part of the domain where the cells intersect the vanishing neighbourhood;
2.  $\Omega_0$ , representing the part of the domain where the cells do not intersect the vanishing neighbourhood.

Applying the divergence theorem twice to equations (6) and (7) in the domains  $\Omega_0$  and  $(\Omega_s - V_\epsilon)$  with the limit taken as  $\epsilon \rightarrow 0$  and neglecting surface integrals (for a rigid body), equations (6) and (7) can be expressed as:

$$\begin{aligned} \hat{p}_a(\mathbf{x}, \omega) &= \lim_{\epsilon \rightarrow 0} \int_{(\Omega_s - V_\epsilon)} \hat{T}_{ij}(\mathbf{y}, \omega) \frac{\partial^2 \hat{G}_h(\mathbf{x}, \mathbf{y})}{\partial y_i \partial y_j} d\mathbf{y} \\ &+ \int_{\Omega_0} \hat{T}_{ij}(\mathbf{y}, \omega) \frac{\partial^2 \hat{G}_h(\mathbf{x}, \mathbf{y})}{\partial y_i \partial y_j} d\mathbf{y} \end{aligned} \quad (8)$$

$$\begin{aligned}
 \hat{q}_{a,k}(\mathbf{x}, \omega) &= \lim_{\varepsilon \rightarrow 0} \int_{(\Omega_S - V_\varepsilon)} \hat{T}_{ij}(\mathbf{y}, \omega) \frac{\partial^3 \hat{G}_h(\mathbf{x}, \mathbf{y})}{\partial y_i \partial y_j \partial x_k} d\mathbf{y} \\
 &+ \int_{\Omega_0} \hat{T}_{ij}(\mathbf{y}, \omega) \frac{\partial^3 \hat{G}_h(\mathbf{x}, \mathbf{y})}{\partial y_i \partial y_j \partial x_k} d\mathbf{y} \quad (9)
 \end{aligned}$$

Evaluation of the incident field on a body within the discretised acoustic source region requires evaluation of strongly singular and hypersingular volume integrals. In what follows, these singular volume integrals are regularised using the singularity subtraction technique of Guiggiani *et al.* (1990, 1992). The application of this technique to strongly singular volume integrals is given by Guiggiani and Gigante (1990) and applied to flow noise sources by Croaker *et al.* (2012). Hypersingular volume integrals are also considered here. Furthermore, close to the body are many near-singular volume integrals which can require a large number of integration points to achieve an accurate solution. To alleviate this problem, the polynomial transformation of Telles (1987) is applied to these near-singular volume integrals.

### Mapping to Intrinsic Coordinates

To facilitate efficient evaluation of equations (8) and (9) using numerical integration, all cells are mapped onto a reference cell in intrinsic coordinates. These intrinsic coordinates are denoted by  $\xi = (\xi, \eta, \zeta)$ . In the present work, a trilinear mapping is used. This allows the Cartesian coordinates of any point,  $\mathbf{y}$ , to be calculated as follows:

$$\mathbf{y}(\xi) = \sum_m M^m(\xi) \mathbf{y}^m \quad (10)$$

where  $m$  represents the nodes used to define the geometry of the cells,  $M^m(\xi)$  are the geometric shape functions of the cells expressed in intrinsic coordinates and  $\mathbf{y}^m$  are the Cartesian coordinates of the  $m^{\text{th}}$  node. During the mapping process, each cell in  $\Omega_0$  and  $\Omega_S$  map onto regions  $\Omega_{0R}$  and  $\Omega_{SR}$ , respectively, in intrinsic coordinates using trilinear shape functions. In intrinsic coordinates, equations (8) and (9) can be expressed as:

$$\begin{aligned}
 \hat{p}_a(\mathbf{x}, \omega) &= \\
 \lim_{\varepsilon \rightarrow 0} \int_{(\Omega_{SR} - \sigma_\varepsilon)} \hat{T}_{ij}(\mathbf{y}(\xi), \omega) \frac{\partial^2 \hat{G}_h(\mathbf{x}, \mathbf{y}(\xi))}{\partial y_i \partial y_j} J(\xi) d\xi d\eta d\zeta \\
 &+ \int_{\Omega_{0R}} \hat{T}_{ij}(\mathbf{y}(\xi), \omega) \frac{\partial^2 \hat{G}_h(\mathbf{x}, \mathbf{y}(\xi))}{\partial y_i \partial y_j} J(\xi) d\xi d\eta d\zeta \quad (11)
 \end{aligned}$$

$$\begin{aligned}
 \hat{q}_{a,k}(\mathbf{x}, \omega) &= \\
 \lim_{\varepsilon \rightarrow 0} \int_{(\Omega_{SR} - \sigma_\varepsilon)} \hat{T}_{ij}(\mathbf{y}(\xi), \omega) \frac{\partial^3 \hat{G}_h(\mathbf{x}, \mathbf{y}(\xi))}{\partial y_i \partial y_j \partial x_k} J(\xi) d\xi d\eta d\zeta \\
 &+ \int_{\Omega_{0R}} \hat{T}_{ij}(\mathbf{y}(\xi), \omega) \frac{\partial^3 \hat{G}_h(\mathbf{x}, \mathbf{y}(\xi))}{\partial y_i \partial y_j \partial x_k} J(\xi) d\xi d\eta d\zeta \quad (12)
 \end{aligned}$$

where  $J(\xi)$  is the Jacobian of the transformation from Cartesian to intrinsic coordinates for the cells. The first terms on the right hand side of equations (11) and (12) are singular and cannot be evaluated by standard numerical integration. Instead, the regularisation technique proposed by Guiggiani *et al.* (1990, 1992) is used to subtract the singularity from the integral. The singular part of the integral is solved semi-analytically and the remaining terms are integrated using standard Gaussian quadrature schemes. This regularisation scheme is outlined in the proceeding section.

The second terms on the right hand side of equations (11) and (12) do not contain the singularity and hence can be evaluated

using standard numerical integration techniques. However it is possible that the singularity may be very close to cells in this region. In such ‘near-singular’ situations, a large number of integration points may be required to achieve an accurate result. The self-adaptive polynomial transformation technique of Telles (1987) is used to evaluate these near singular cases and this procedure is outlined in a later section. Gauss-Legendre quadrature is used to evaluate all regular integrals in this work.

### Regularisation of Singular Integrals

As the first terms on the right hand side of equations (11) and (12) are singular, they cannot be evaluated by standard numerical integration. To remove these singularities, a coordinate transformation to spherical coordinates,  $\sigma = (\sigma, \theta, \phi)$ , is employed. These spherical coordinates are centred at  $\xi_0 = (\xi_0, \eta_0, \zeta_0)$ , corresponding to the image of  $\mathbf{x}$  in intrinsic coordinates, and are given by

$$\xi = \xi_0 + \sigma \cos \theta \sin \phi, \quad \eta = \eta_0 + \sigma \sin \theta \sin \phi, \quad \zeta = \zeta_0 + \sigma \cos \phi \quad (13)$$

where  $\sigma$  is the radius,  $\theta$  is the azimuth angle and  $\phi$  is the zenith angle. The Jacobian of the transformation from intrinsic to spherical coordinates results in the following relationship

$$d\xi d\eta d\zeta = \sigma^2 \sin \phi d\sigma d\theta d\phi \quad (14)$$

This spherical coordinate transformation weakens the singularity of equations (11) and (12) to  $O(\sigma^{-1})$  and  $O(\sigma^{-2})$ , respectively. To regularise the remaining singularity, the singularity subtraction technique of Guiggiani *et al.* (1990, 1992) is implemented. After application of this regularisation technique, the singular integrals of equations (11) and (12) can be calculated accurately using Gaussian quadrature.

### Treatment of Near-Singular Integrals

Near-singular integrals are regular integrals and can hence be solved numerically using standard quadrature schemes. However, when the field point is located close to a cell, the number of integration points required to achieve an accurate solution becomes large. Coordinate transformation techniques cluster the integration points towards the singularity. Using a self-adaptive polynomial transformation technique (Telles, 1987), this integration point clustering is related to the distance between a field point and a cell. Hence, as the distance increases, the distribution of integration points within the element reverts to normal. This allows the technique to be easily applied to all near-singular integrals within the model.

### Transient Laminar CFD Simulation

To demonstrate the CFD-BEM coupling technique, laminar vortex shedding from a cylinder of diameter  $D$  is simulated at a Reynolds number  $Re_D = 100$  and Mach number  $M = 0.02$ . At this Reynolds number the flow is in the laminar unsteady regime and is predominantly two-dimensional, with negligible spanwise contribution (Martínez-Lera and Schram, 2008). Hence, only a two-dimensional CFD simulation is considered here. A two-dimensional circular domain around the cylinder has been modelled and analysed using ESI Group’s CFD-ACE+ software package. The velocity-pressure form of the incompressible Navier-Stokes equations are solved by CFD-ACE+ in this instance. The incompressible Navier-Stokes equations are

given by:

$$\begin{aligned} \rho_0 \frac{\partial (u_x)}{\partial t} + \rho_0 \nabla \cdot (\mathbf{u}u_x) &= -\frac{\partial p}{\partial x} + \nabla \cdot (\mu \nabla u_x) + S_{M_x} \\ \rho_0 \frac{\partial (u_y)}{\partial t} + \rho_0 \nabla \cdot (\mathbf{u}u_y) &= -\frac{\partial p}{\partial y} + \nabla \cdot (\mu \nabla u_y) + S_{M_y} \\ \rho_0 \frac{\partial (\rho u_z)}{\partial t} + \rho_0 \nabla \cdot (\mathbf{u}u_z) &= -\frac{\partial p}{\partial z} + \nabla \cdot (\mu \nabla u_z) + S_{M_z} \\ \nabla \cdot \mathbf{u} &= 0 \end{aligned} \quad (15)$$

where  $\mathbf{u} = (u_x, u_y, u_z)$  is the velocity vector and  $S_{M_x}$ ,  $S_{M_y}$  and  $S_{M_z}$  are momentum source terms in the  $x$ ,  $y$  and  $z$  directions, respectively. CFD-ACE+ uses an iterative, segregated solution method with the pressure-velocity coupling handled using the SIMPLEC algorithm.

The model used for the CFD simulation is shown in Figure 2, with the mesh topology in the vicinity of the cylinder inset. The interior of the computational domain extends radially for  $25D$ . A sponge layer extends radially for an additional  $20D$ . The interior domain contains 71,760 quadrilateral cells, with a cell spacing adjacent to the cylinder of  $0.005D$ . The cell distribution is biased so that the wake region contains a high cell density to resolve the vortices shed from the cylinder. The sponge layer contains an additional 6,960 quadrilateral cells. The cell size on either side of the interface between the interior domain and sponge layer is uniform, with the cells in the sponge layer then growing rapidly in the radial direction.

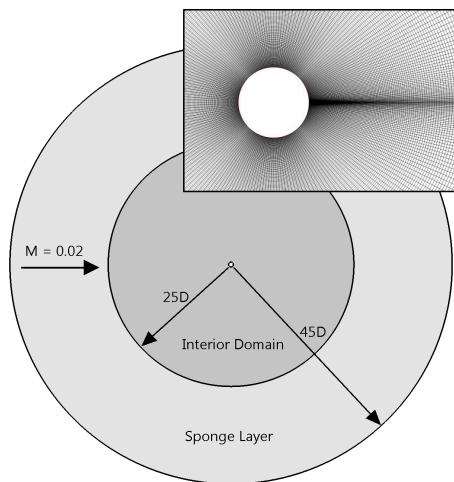


**Figure 2:** Domain shape and size for CFD analysis

The viscosity in the sponge layer has been artificially increased by a factor of 35 to damp out the fluctuations in the velocity field in an attempt to force the acoustic source terms to zero at the boundary. A steady state simulation was performed with the converged solution used as the initial condition of the transient simulation. The simulations were second order accurate in time and space, with a central difference scheme used for the spatial discretisation and a Crank-Nicholson scheme used for the temporal discretisation. The transient simulation was executed with a non-dimensionalised time step size of  $\Delta t \frac{U_\infty}{D} = 2.99E-3$ , where  $U_\infty$  is the free stream velocity. This corresponds to a Courant-Fredrichs-Lewy (CFL) number of approximately 0.6. The simulation was allowed to progress until the flow field achieved periodicity. Recording of the acoustic source data commenced after this periodicity had been attained and data from eight vortex shedding periods was obtained.

## BEM Model and Incident Acoustic Field

The two-dimensional BEM model consisted of 40 linear one-dimensional elements around the circumference of the cylinder, with the vertices placed on the cylinder in  $9^\circ$  increments with  $0^\circ$  aligned with the direction of fluid flow. The vertices of these BEM elements also represent the field points used to calculate the incident acoustic field. The method presented here has been developed for three-dimensional applications and hence the acoustic propagation was carried out in three dimensions. An artificial thickness of  $0.1D$  was assigned to the two-dimensional CFD cells and 100 identical copies of these sources were extruded out of the plane of the flow. Symmetry about the plane of the flow was taken into account, resulting in a source region with an out-of-plane span of  $20D$ . Simulations were also performed using smaller artificial thicknesses and longer out-of-plane spans were also considered, however these had negligible impact on the incident field on the cylinder and the far-field sound pressure level.

## Far-field Sound Pressure Level

The field points were placed on a circle of radius  $6000D$  centred on the cylinder in  $9^\circ$  increments with  $0^\circ$  aligned with the direction of fluid flow. The direct radiation from the volume quadrupole sources to the far-field has not been considered here. Only the scattered acoustic pressure is recorded at the far-field locations. It should be noted that this scattered acoustic pressure includes the radiation by the viscous shear stress dipoles, which have been evaluated using Curle's analogy (Curle, 1955).

## RESULTS AND DISCUSSION

### Hydrodynamic Analysis

The hydrodynamic analysis has been presented previously by the authors (Croaker *et al.*, 2013). Figure 3 shows a plot of the vorticity in the flow field at one instance in time, with the black arc representing the boundary of the sponge layer. The vorticity generated at the cylinder surface is shed from the cylinder and travels downstream as vortex pairs. Figure 3 shows that the sponge layer is effective in damping out the vorticity before reaching the downstream boundary.

Figure 4 shows the frequency spectra of the fluctuating lift and drag forces exerted on the cylinder. The fundamental vortex shedding frequency occurs at Strouhal number  $S_r = 0.165$ . This figure also illustrates that peaks of the fluctuating lift force occur at odd harmonics of the vortex shedding frequency and peaks of the drag force occur at even harmonics.

Table 1 compares the results obtained with the present hydrodynamic simulation with reference solutions from literature. A more detailed discussion of these results can be found in Croaker *et al.* (2013). Table 1 shows a comparison of the Strouhal number, time averaged drag coefficient  $\bar{C}_D$ , peak-to-peak lift coefficient  $\Delta C_L$  and time averaged base-pressure coefficient  $-\bar{C}_{p_b}$ . The reference values are taken from the experimental results of Fey *et al.* (1998) [1], empirical expressions derived by Norberg (2001) [2] and the numerical simulations of Posdziech and Grundmann (2007) [3] and Martínez-Lera and Schram (2008) [4].

### Incident Acoustic Field

The incident acoustic field was calculated using the regularised forms of equations (11) and (12). The acoustic pressure and pressure gradient incident on the cylinder, normalised by  $\rho_0 U_\infty^2$ , at the vortex shedding frequency are shown in Figure 5. The

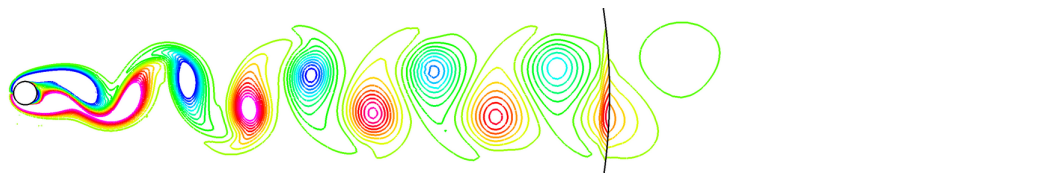


Figure 3: Vortices in wake of cylinder. Dimensionless vorticity,  $\gamma$ , contours from  $\gamma_{min} = -1$  to  $\gamma_{max} = 1$  with an increment of 0.1

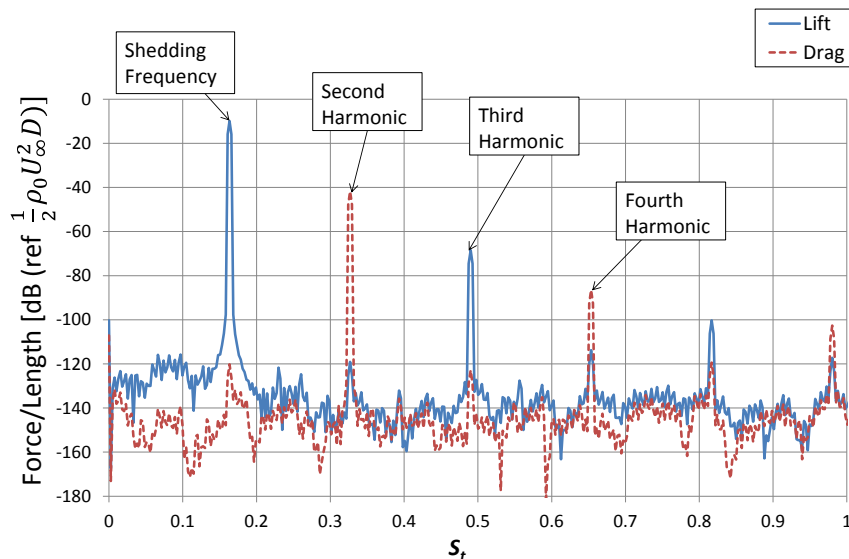


Figure 4: Frequency spectra of the lift and drag forces

Table 1: Comparison of the hydrodynamic results with reference values

	$S_t$	$\bar{C}_D$	$\Delta C_L$	$-\bar{C}_{Pb}$
Refs. [1,2]	0.164 <sup>Ref.[1]</sup>	—	0.643 <sup>Ref.[2]</sup>	—
Ref. [3]	0.165	1.331	0.647	0.717
Ref. [4]	0.170	1.393	0.686	0.787
Present	0.165	1.326	0.640	0.698

symmetry of both the pressure and pressure gradient about the direction of flow is clearly observed.

### Far-Field Directivity of the Scattered Field

The incident acoustic field was applied to the BEM model of the cylinder and solved using the AEBEM2 subroutine of Kirkup (1998). The far-field directivity of the sound pressure field scattered by the cylinder, normalised by  $\rho_0 U_\infty^2$ , is shown in Figure 6. Figure 6 also shows the contributions of the viscous shear stress dipoles and the total far-field sound pressure. This total sound pressure field is compared with the results obtained using Curle’s analogy by Croaker *et al.* (2013). The far-field directivity and magnitude of the total sound pressure is very similar between the present work and that obtained using Curle’s analogy. The contribution from the viscous shear stress is significant for this low Reynolds number, as discussed by Khalighi (2010).

### CONCLUSIONS

A CFD-BEM coupling technique has been developed to predict the scattering of flow induced acoustic waves by a rigid body immersed in the flow. The method extracts the acoustic sources based on Lighthill’s analogy from incompressible CFD data and computes the propagation of the resulting acoustic waves from the flow noise sources to the surface of the body. The

incident acoustic field on the body is then applied to an existing BEM solver to predict the scattered sound pressure in the far-field. This CFD-BEM coupling technique has been applied to predict the scattering of sound waves produced by laminar vortex shedding from a two-dimensional cylinder at a Reynolds number,  $Re_D = 100$  and Mach number,  $M = 0.02$ . The total far-field sound pressure level predicted with the present method, which includes both the scattered field and the radiation due to the viscous shear stress dipoles, compares well with results from the literature obtained using Curle’s analogy.

### ACKNOWLEDGEMENTS

Funding for this work from the Maritime Platforms Division of the Defence Science and Technology Organisation is gratefully acknowledged.

### REFERENCES

Crighton, DG 1993, *Computational Aeroacoustics for Low Mach Number Flows*, Springer-Verlag, Berlin / New York / Heidelberg, pp. 50–68.  
 Croaker, P, Kessissoglou, N and Marburg, S 2012, ‘A unified approach to predict near and far-field acoustic pppressure from Lighthill’s Analogy’, *18th Australasian Fluid Mechanics Conference*, Launceston, Australia.  
 Croaker, P, Marburg, S, Kinns, R and Kessissoglou, N 2013, ‘A fast low-storage method for evaluating Lighthill’s volume quadrupoles’, *AIAA Journal*, vol. 51, pp. 867–884.  
 Curle, N 1955, ‘The influence of solid boundaries upon aerodynamic sound’, *Proceedings of the Royal Society of London A*, vol. 231, pp. 505–514.  
 Fey, U, König, M and Eckelmann, H 1998, ‘A new Strouhal–Reynolds-number relationship for the circular cylinder in the range  $47 < Re < 2 \times 10^5$ ’, *Physics of Fluids*, vol. 10, 7, pp. 1547–1549.

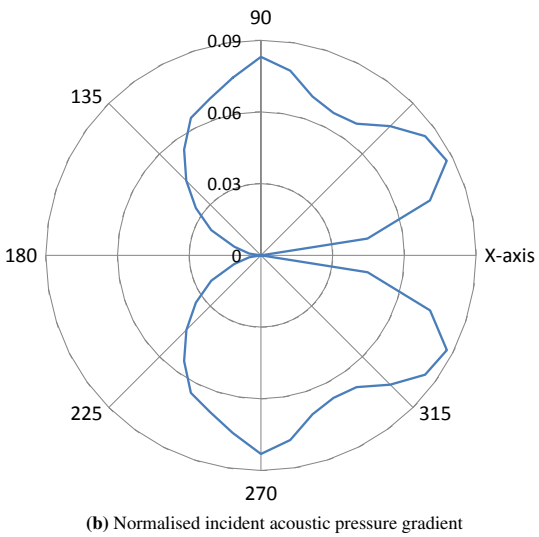
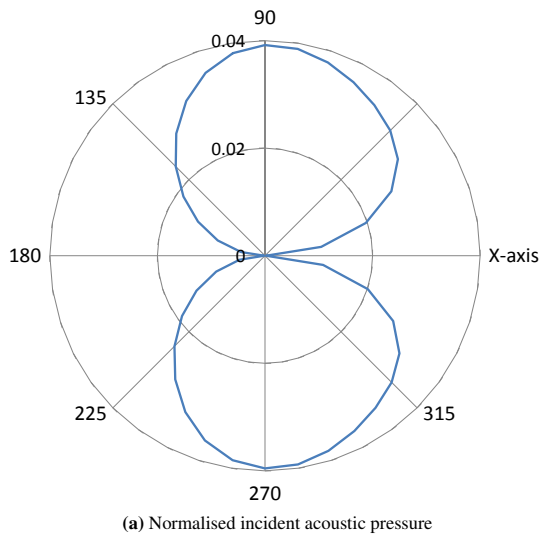


**Figure 5:** Directivity of the normalised acoustic field incident on the cylinder, at the vortex shedding frequency

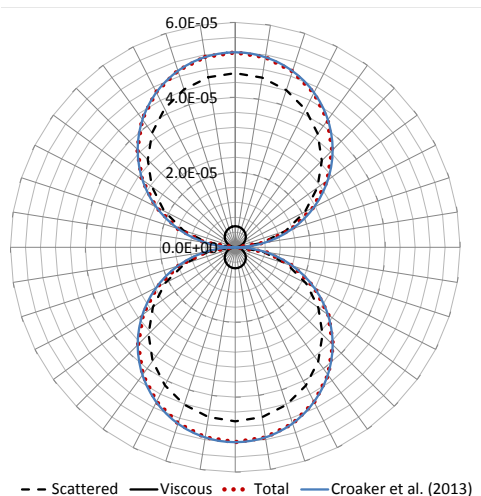


**Figure 6:** Directivity of the normalised scattered pressure amplitude at  $r = 6000D$  at the vortex shedding frequency

Gloerfelt, X, Pérot, F, Bailly, C and Juvé, D 2005, 'Flow-induced cylinder noise formulated as a diffraction problem for low Mach numbers', *Journal of Sound and Vibration*, vol. 287, pp. 129–151.

Guiggiani, M and Gigante, A 1990, 'A general algorithm for multidimensional Cauchy principal value integrals in the boundary element method', *ASME Journal of Applied Mechanics*, vol. 57, pp. 906–915.

Guiggiani, M, Krishnasamy, G, Rudolph, TJ and Rizzo, FJ 1992, 'A general algorithm for the numerical solution of hypersingular boundary integral equations', *ASME Journal of Applied Mechanics*, vol. 59, pp. 604–614.

Khalighi, Y 2010, 'Computational Aeroacoustics of Complex Flows at Low Mach Number', PhD thesis, Stanford University.

Khalighi, Y, Mani, A, Ham, F and Moin, P 2010, 'Prediction of sound generated by complex flows at low Mach numbers', *AIAA Journal*, vol. 48, 2, pp. 306–316.

Kirkup, SM 1998, *The Boundary Element Method in Acoustics*, Integrated Sound Software.

Lighthill, MJ 1952, 'On sound generated aerodynamically, I. General theory', *Proceedings of the Royal Society A*, vol. 211, pp. 564–587.

Lighthill, MJ 1954, 'On sound generated aerodynamically, II. Turbulence as a source of sound', *Proceedings of the Royal Society A*, vol. 222, pp. 1–32.

Martínez-Lera, P and Schram, C 2008, 'Correction techniques for the truncation of the source field in acoustic analogies', *Journal of the Acoustical Society of America*, vol. 124, pp. 3421–3429.

Norberg, C 2001, 'Flow around a circular cylinder: Aspects of fluctuating lift', *Journal of Fluids and Structures*, vol. 15, pp. 459–469.

Posdziech, O and Grundmann, R 2007, 'A systematic approach to the numerical calculation of fundamental quantities of the two-dimensional flow over a circular cylinder', *Journal of Fluids and Structures*, vol. 23, pp. 479–499.

Powell, A 1964, 'Theory of vortex sound', *Journal of the Acoustical Society of America*, vol. 36, pp. 177–195.

Schram, C 2009, 'A boundary element extension of Curle's analogy for non-compact geometries at low-Mach numbers', *Journal of Sound and Vibration*, vol. 322, pp. 264–281.

Telles, JCF 1987, 'A self-adaptive co-ordinate transformation for efficient numerical evaluation of general boundary element integrals', *International Journal for Numerical Methods in Engineering*, vol. 24, pp. 959–973.